ACS APPLIED MATERIALS & INTERFACES

Research Article

www.acsami.org

# Three-Dimensional Interconnected Network of Graphene-Wrapped Porous Silicon Spheres: In Situ Magnesiothermic-Reduction Synthesis and Enhanced Lithium-Storage Capabilities

Ping Wu,* Hui Wang, Yawen Tang, Yiming Zhou,* and Tianhong Lu

Jiangsu Key Laboratory of New Power Batteries, Jiangsu Collaborative Innovation Center of Biomedical Functional Materials, School of Chemistry and Materials Science, Nanjing Normal University, Nanjing 210023, P. R. China

**ABSTRACT:** A novel type of 3D porous Si−G micro/nanostructure (i.e., 3D interconnected network of graphene-wrapped porous silicon spheres, Si@G network) was constructed through layer-by-layer assembly and subsequent in situ magnesiothermic-reduction methodology. Compared with bare Si spheres, the as-synthesized Si@G network exhibits markedly enhanced anodic performance in terms of specific capacity, cycling stability, and rate capability, making it an ideal anode candidate for high-energy, long-life, and high-power lithium-ion batteries.

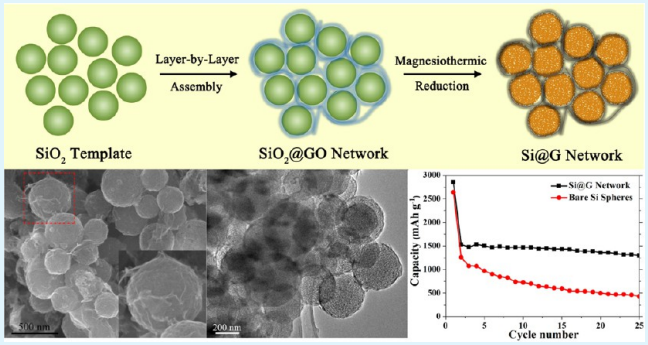


**KEYWORDS:** *lithium-ion batteries, anodes, silicon, graphene, interconnected network, magnesiothermic reduction*

## 1. INTRODUCTION

Owing to their high theoretical capacity and natural abundance, silicon materials have been considered to be the most promising anode candidates for advanced lithium-ion batteries (LIBs).[1] However, the practical application of silicon anodes has been greatly impeded, primarily because of their huge volume fluctuation during lithium insertion/extraction, resulting in progressive pulverization, loss of electrical continuity, and fast capacity fading.[2,3] Moving from conventional bulk to various micro/nanostructures can solve the aforementioned issues to a large extent owing to their high surface area and large pore volume.[1−14] However, significant challenges still remain for these single-component silicon anodes in terms of cycling stability and rate capability, which originates from their poor structural stability and low intrinsic electrical conductivity.

To overcome these issues, extensive research has been concentrated on constructing hybrid anodes by integrating micro/nanosilicon with carbon matrixes.[15−25] Among them, graphene has been proven to be the primary candidate for use as the buffering/conducting matrix for silicon anodes owing to its exceptional physicochemical properties in terms of flexibility, mechanical strength, and electrical conductivity.[26] For example, a series of graphene and its self-assembled scaffolds-supported silicon anodes exhibit improved structural stability and charge-transport capability and thus enhanced lithium-storage performance.[15−21] Among them, the self-assembled three-dimensional (3D) porous graphene scaffolds possess the structural features of both nanoscale building blocks and microsized assemblies and thus demonstrate enhanced host capability, strain accommodation, and charge-transport capabilities.[15,27−30] Therefore, the micro/nanohybrids of silicon and 3D porous graphene scaffolds are anticipated to display further enhanced lithium-storage capabilities and to meet the performance requirements of advanced LIBs for electric vehicles and electrical grids.

Herein, a novel type of 3D porous Si−G micro/nanostructure (i.e., 3D interconnected network of graphene-wrapped porous silicon spheres, Si@G network) was constructed through layer-by-layer assembly and subsequent in situ magnesiothermic-reduction methodology. When examined as a potential anode material for LIBs, the as-synthesized Si@G network exhibits markedly enhanced lithium-storage capabilities in terms of specific capacity, cycling stability, and rate capability.

## 2. EXPERIMENTAL SECTION

**2.1. Synthesis of the Si@G Network.** First, $SiO_2$ sphere templates with a diameter of ca. 300 nm were synthesized via a modified Stober method.[31] Then, the 3D interconnected network of graphene oxide (GO) sheets-wrapped $SiO_2$ spheres ($SiO_2$@GO network) was prepared through a layer-by-layer assembly approach based on electrostatic attraction between charged species. $SiO_2$ templates were modified with poly(diallyldimethylammonium chloride) (PDDA) and poly(sodium 4-styrenesulfonate) (PSS) in sequence, yielding positively charged PDDA/PSS/PDDA-modified $SiO_2$ templates.[32] Subsequently, the polyelectrolyte-modified $SiO_2$ templates and GO (2:1 w/w) were dispersed in distilled water, stirred for 6 h, washed with distilled water and ethanol, and then dried at 80 °C in air. Finally, the as-synthesized $SiO_2$@GO network was mixed with Mg

Received: December 12, 2013
Accepted: January 31, 2014
Published: January 31, 2014

  

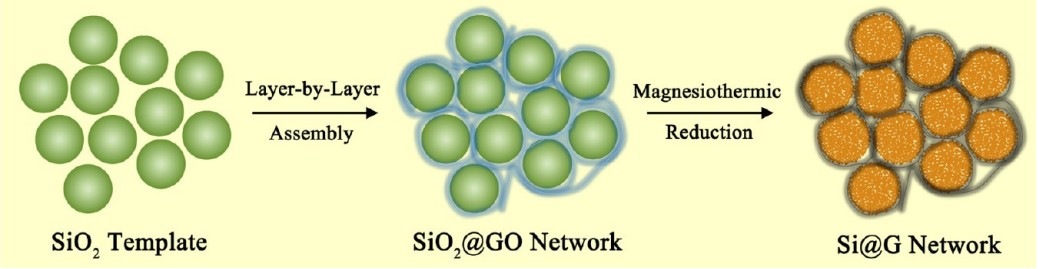


**Figure 1.** Schematic illustration for the synthesis of the Si@G network.

powder in a mass ratio of 1:1 and then annealed at 650 °C for 6 h under Ar. Subsequently, the Si@G network was obtained by etching the formed MgO and possible $Mg_2Si$ byproduct with a 1 M HCl solution.

**2.2. Characterization.** The morphology, composition, and structure of the samples were characterized by scanning electron microscopy (SEM, JEOL JSM-7600F), transmission electron microscopy (TEM, Hitachi H-7650, 120 kV), and high-resolution transmission electron microscopy (HRTEM, JEOL JEM-2010F, 200 kV) coupled with an energy-dispersive X-ray spectrometer (EDX, Thermo Fisher Scientific). X-ray powder diffraction (XRD) measurements were performed with Rigaku D/max-rC diffractometer using Cu K$\alpha$ radiation ($\lambda$ = 0.15406 nm) and operating at 45 kV and 100 mA. The differential scanning calorimetry and thermogravimetric analysis (DSC-TGA) was carried out on a Netzsch STA 449C thermal analyzer at a heating rate of 10 °C $min^{-1}$ in air.

**2.3. Electrochemical Measurements of the Si@G Network.** Electrochemical tests were performed by 2025 type coin cells that were assembled in an Ar-filled glovebox (IL-2GB, Innovative Technology). The anodes were constructed as follows: 70 wt % Si@G network, 15 wt % Super P carbon black, and 15 wt % poly(vinylidene fluoride) (PVDF) in *N*-methyl-2-pyrrolidene (NMP) were mixed, and the slurry was coated on the surface of copper foam at room temperature and dried under vacuum at 120 °C for 12 h. The graphene matrix was considered to be part of the active material when calculating the specific capacities of Si@G network, and the amount of active material loading on each copper foam was ca. 2 mg. The counter electrode was lithium foil, and the electrolyte solution was 1 M $LiPF_6$ in ethylene carbonate (EC) and dimethyl carbonate (DMC) (1:1 v/v). Last, the cells were aged for 12 h before measurements. A galvanostatic cycling test of the assembled cells was carried out on a Land CT2001A system in the potential range of 0.01−1.2 V. Cyclic voltammtery (CV) measurements were recorded on a CHI 660C electrochemical workstation in the potential range of 0.0−1.2 V at a scan rate of 0.1 mV $s^{-1}$. The voltages mentioned herein were referenced to the $Li^+$/Li redox couple. All of the electrochemical measurements were conducted at 20 °C.

## 3. RESULTS AND DISCUSSION

Figure 1 depicts the schematic diagram for the formation of the Si@G network. As observed, the $SiO_2$ spherical templates were first wrapped by GO sheets via a facile layer-by-layer technique based on electrostatic attraction. The strong electrostatic attraction between positively charged PDDA/PSS/PDDA-modified $SiO_2$ templates and negatively charged GO sheets facilitates the uniform, continuous, and flexible coating of GO on $SiO_2$ templates, resulting in 3D interconnected $SiO_2$@GO network. After an in situ magnesiothermic-reduction procedure, the $SiO_2$ spherical templates were converted to porous Si spheres, and the GO scaffold could be transformed to a graphene network, yielding a 3D interconnected porous Si@G network. Figure 2 shows the XRD patterns of the corresponding samples. As observed, the crystalline phase from Si@G network (curve c) can be assigned to cubic Si

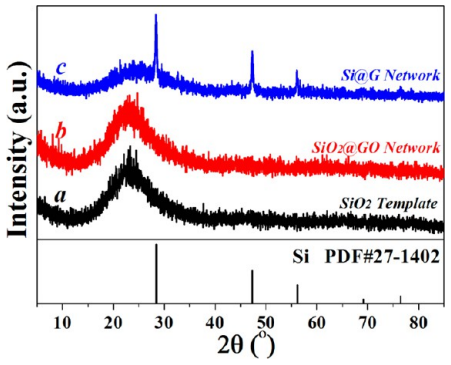


**Figure 2.** XRD patterns of $SiO_2$ spheres (curve a), $SiO_2$@GO network (curve b), and Si@G network (curve c).

(JCPDS: 27-1402) with an average crystalline size of ca. 10 nm, whereas the $SiO_2$ template and $SiO_2$@GO intermediate are amorphous in nature (curves a and b).[15]

The morphology and structure of the $SiO_2$@GO network were further characterized by SEM and TEM (Figure 3). The observed wrinkles and folds over the entire surface of $SiO_2$ spheres are characteristic of GO sheets, confirming the full encapsulation of $SiO_2$ templates by GO sheets. In addition, the GO-wrapped $SiO_2$ spheres could be easily bridged by GO sheets owing to their relatively larger lateral sizes, yielding a 3D interconnected hybrid network. The strong electrostatic interaction between oppositely charged $SiO_2$ and GO together with the flexibility of GO can be responsible for the formation of the unique $SiO_2$@GO network. Moreover, a pure graphene scaffold can be obtained by removing the $SiO_2$ cores in the $SiO_2$@GO network and subsequent chemical reduction of GO to graphene (Figure 4). As observed, the graphene scaffold exists in the form of a 3D interconnected network composed of self-assembled graphene hollow spheres, further confirming the uniform and continuous coating of GO sheets on $SiO_2$ templates in the $SiO_2$@GO network. Additionally, the 3D interconnected graphene network could serve as promising electrodes and/or supporting matrixes for advanced electrodes in energy storage and conversion systems owing to the enhanced host capability, structural stability, and electrical conductivity.[33,34]

The as-prepared $SiO_2$@GO network could be in situ converted into a Si@G network via a magnesiothermic-reduction methodology, which was pioneered by Bao et al. and has been regarded as an economic and scalable approach for porous silicon materials.[8−15] Figure 5 displays the morphological, structural, and compositional characterizations of the Si@G network. As observed from the SEM and TEM images, the Si−G building block is bridged by graphene matrix and thus the 3D interconnected structure of the $SiO_2$@GO

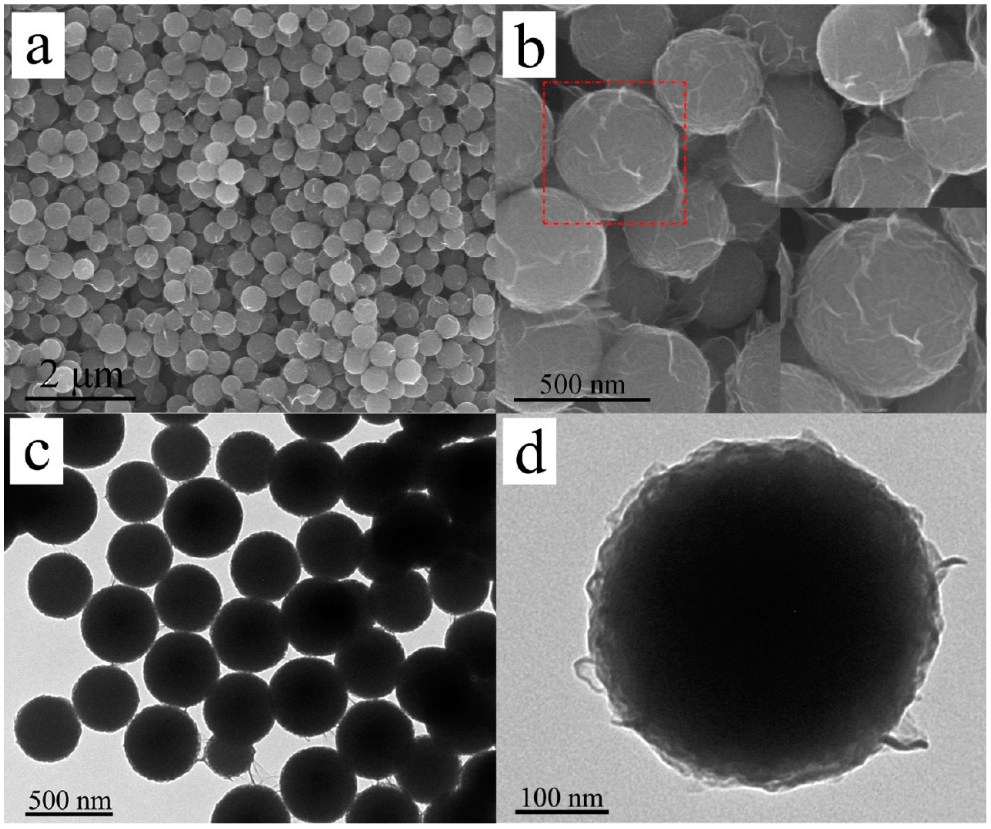


**Figure 3.** Morphological and structural characterizations of the $SiO_2$@GO network: (a, b) SEM images and (c, d) TEM images.

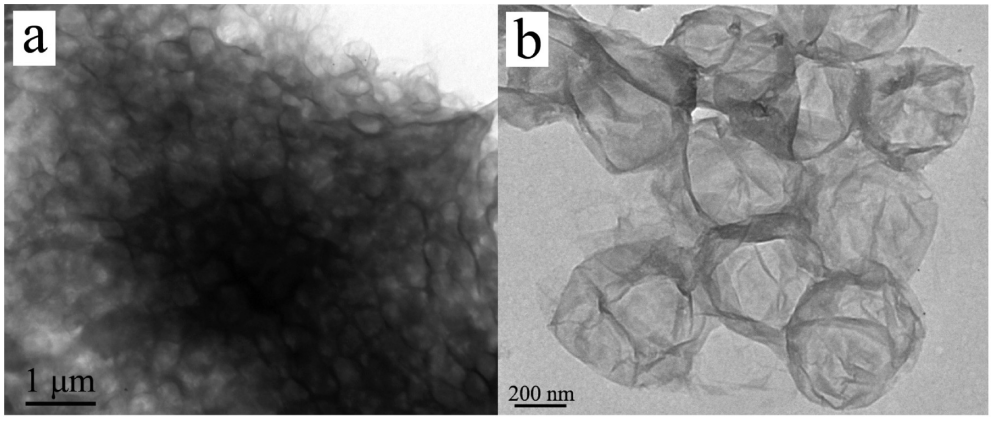


**Figure 4.** (a, b) TEM images of the 3D interconnected graphene network at different magnifications.

network is well-retained in the Si@G network. The magnified TEM image (Figure 5d) clearly reveals that its Si−G building block exists in the form of mesoporous Si spheres fully wrapped by graphene matrix. Such mesoporosity of Si spheres is mainly created by selective acid etching of the MgO and $Mg_2Si$ byproduct[10,12,15] and is beneficial for the strain relaxation and contact with electrolyte and thus the improved anodic performance of the Si@G network. Moreover, the HRTEM image of an edge part in a Si@G sphere show that the Si nanocrystals are well-encapsulated within the outer graphene matrix and the observed lattice fringe in the core region with a lattice spacing of 0.31 nm originates from the (111) plane of cubic Si (Figure 5e). Figure 5f shows the TEM image of several Si@G spheres along with their elemental maps of C (yellow), Si (purple), and their overlap. As observed, Si is mainly distributed within the core region, whereas C is homogeneously distributed in the chosen area. The TEM-EDX elemental mapping results further confirm the formation of the Si@G network. For comparison, bare Si spheres were obtained via magnesiothermic reduction of $SiO_2$ spheres instead of the $SiO_2$@GO network with the other conditions unchanged. As observed, the bare Si product exists in the form of isolated mesoporous spheres rather than interconnected networks (Figure 6).

DSC-TGA was performed to determine quantitatively the graphene content presented in the Si@G network (Figure 7). As can be seen, the initial weight loss up to 150 °C together with an endothermic peak at 93.3 °C corresponds to the removal of physically adsorbed water, whereas the weight loss between 400 and 700 °C accompanied with an exothermic peak

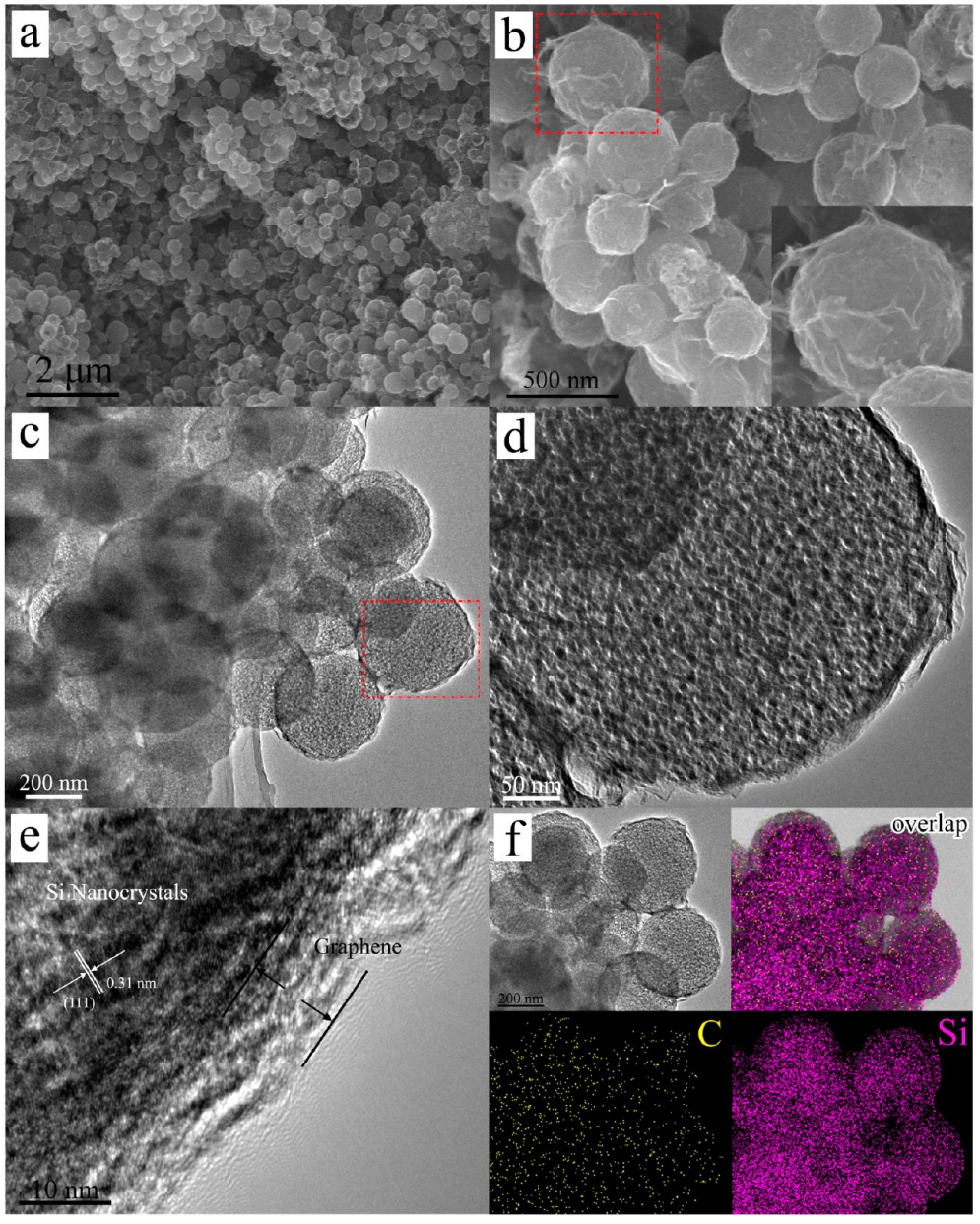


**Figure 5.** Morphological, structural, and compositional characterizations of the Si@G network: (a, b) SEM images, (c, d) TEM image, (e) HRTEM image, and (f) TEM-EDX elemental mapping of C (yellow), Si (purple), and their overlap.

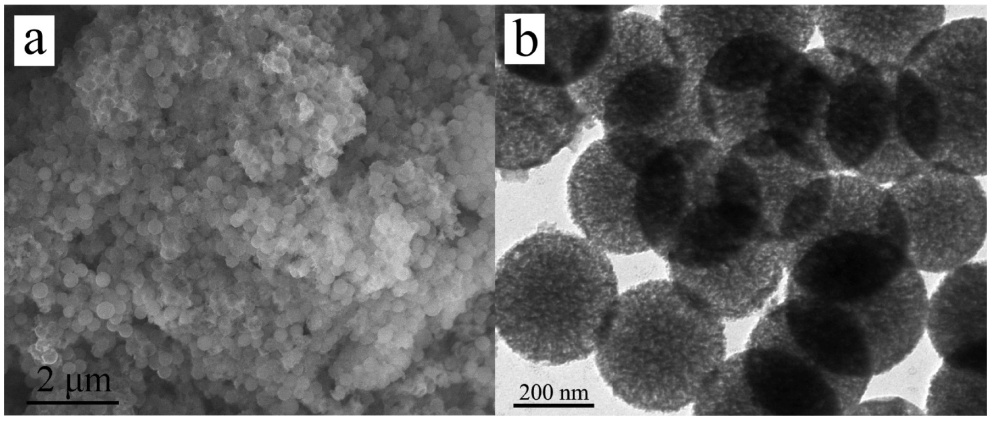


**Figure 6.** SEM and TEM images of bare Si spheres.


dx.doi.org/10.1021/am405725u | ACS Appl. Mater. Interfaces 2014, 6, 3546−3552

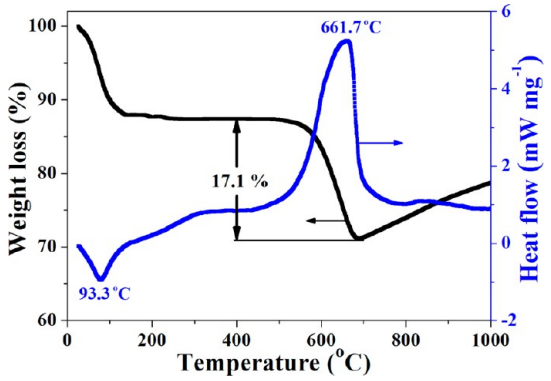


**Figure 7.** DSC-TGA curves of the Si@G network.

at 661.7 °C could be attributed mainly to the combustion of graphene matrix. Additionally, the subsequent weight gain is due to the slight surface oxidation of Si nanocrystals. Thus, the graphene content in the Si@G network is determined to be ca. 17.1% by weight.

Motivated by its microscopic structural features, we investigated the electrochemical behavior of the Si@G network as a potential anode material for lithium storage. For comparison, the lithium-storage performance of bare Si spheres was also examined under the same conditions. Figure 8 shows

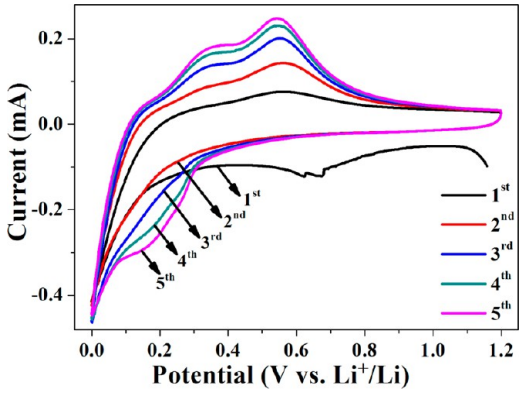


**Figure 8.** CV curves of the Si@G network during the initial five cycles in the potential range of 0.0−1.2 V at a scan rate of 0.1 mV s$^{-1}$.

the first five CV curves of the Si@G network in the potential range of 0.0−1.2 V at a scan rate of 0.1 mV s$^{-1}$. As observed, the profiles of these curves are in accordance with the lithium-storage behavior for Si-based anodes as described previously: electrolyte + $Li^+ + e^- \rightarrow$ solid electrolyte interface (SEI) layer (eq 1); $Si + xLi^+ + xe^- \leftrightarrow Li_xSi$ $(0 \leq x \leq 4.4)$ (eq 2).[1,2] In the first cycle, the cathodic peak at ca. 0.65 V related to the SEI layer disappears in subsequent cycles, indicating the formation of a stable SEI film on the Si@G anode surface.[16] The characteristic pair (cathodic, anodic) of current peaks at (0.0−0.4, 0.36, and 0.53 V) could be attributed to the lithium-insertion/extraction processes described by eq 2. It should be noted that the cathodic peaks located at ca. 0.2 V become more distinct during cycling because of the gradual evolution from crystalline Si to amorphous Si with repeated lithium-insertion/extraction processes.[13−16] Additionally, the intensity of anodic peaks at 0.36 and 0.53 V increases gradually in the initial five cycles, suggesting the existence of probable activating processes in the Si@G network anode.[14−16]

Figure 9a shows the discharge capacities versus cycle number for the Si@G network and bare Si spheres in the potential range of 0.01−1.2 V at a current density of 0.05 C (1 C = 4200 mA g$^{-1}$). As can be seen, the Si@G network exhibits significantly enhanced cycling stability over bare Si spheres, making it an ideal anode candidate for long-life LIBs. After 25 cycles, the Si@G network is able to deliver a high reversible capacity of 1299.6 mA h g$^{-1}$, which is much higher than that of bare Si spheres (431.5 mA h g$^{-1}$). The improved capacity retention of the Si@G network can be ascribed to its unique structrual features of porous spheres, graphene matrix, and 3D interconnected network, which are also beneficial for enhanced charge-transport capability and thus high rate capability. Figure 9b reveals the rate capability of the Si@G network and bare Si spheres at various current densities from 0.05 to 0.1, 0.2, 0.5 C, and finally back to 0.05 C. The observed discharge capacities of the Si@G network vary along with current densities, and the average values change from 1467.5 to 1210.6, 970.7, and 697.8 mA h g$^{-1}$ and finally reversibly recover to 1096.8 mA h g$^{-1}$. In sharp contrast, the discharge capacities of bare Si spheres decrease much more rapidly with the increase of charging/discharging rates. These results demonstrate the markedly improved rate capability of the Si@G network over bare Si spheres, facilitating its application in advanced LIBs with high-power densities. Moreover, the lithium-storage capabilities of the Si@G network could be further improved by optimizing the amount of graphene matrix, utilizing new binders with higher concentrations of carboxylic groups, and so forth.[6,35−37]

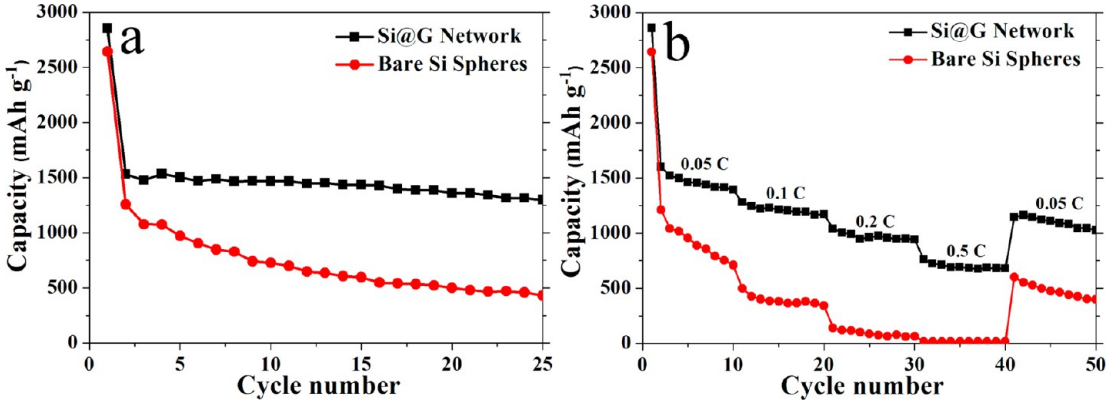


**Figure 9.** Lithium-storage performance of the Si@G network and bare Si spheres: (a) cycling performance and (b) rate capability.

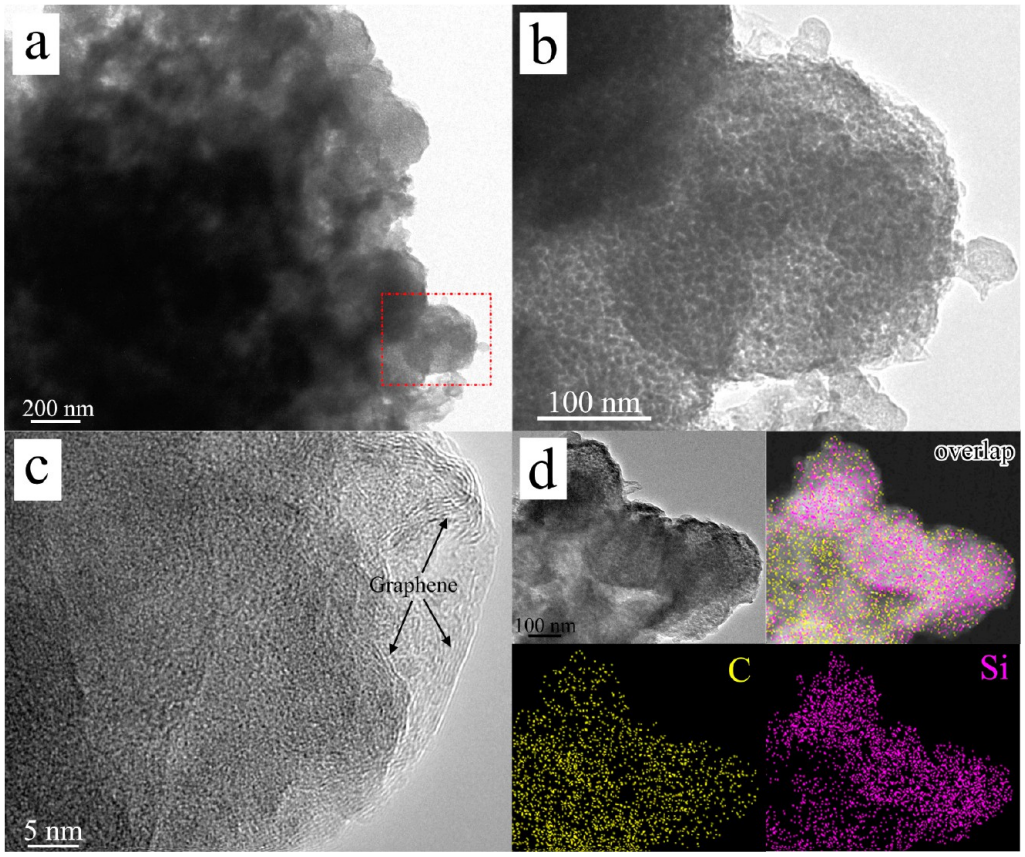


**Figure 10.** Morphological and structural characterizations of the Si@G network in a fully delithiated state (1.2 V vs $Li^+/Li$) after 25 cycles: (a, b) TEM image, (c) HRTEM image, and (d) TEM-EDX elemental mapping of C (yellow), Si (purple), and their overlap.

Figure 10 displays the microscopic structural features of the Si@G network in a fully delithiated state (1.2 V vs $Li^+/Li$) after 25 cycles. As observed from the TEM images, the 3D interconnected network and porous spherical building block are both well-preserved after repeated lithium insertion/extraction, indicating the agglomeration and pulverization of Si nanoparticles could be effectively suppressed (Figure 10a,b). The HRTEM image (Figure 10c) reveals that the Si components are fully encapsulated by graphene matrix and the delithiated Si nanoparticles are amorphous in nature, which is consistent with the CV curves. Moreover, the TEM-EDX elemental mapping demonstrates that the silicon and carbon signals are still evenly distributed within the Si@G spheres, confirming the uniform distribution of silicon components in the delithiated product (Figure 10d). These microscopic structural characterizations of the delithiated product further demonstrate the excellent structural stability of the Si@G network anode during cycling, which plays a key role in the improved lithium-storage capability. Moreover, the proposed synthetic methodology could open up new opportunities for constructing silicon-based micro/nanostructures for further-enhanced lithium-storage capabilities.

## 4. CONCLUSIONS

We have designed and synthesized a novel type of 3D porous Si−G micro/nanostructure (i.e., 3D interconnected network of graphene-wrapped porous silicon spheres, Si@G network) via layer-by-layer assembly and subsequent in situ magnesiothermic-reduction methodology. Owing to its unique structural features, the as-synthesized Si@G network exhibits higher reversible capacity, improved cycling stability, and higher rate capability compared with bare Si spheres. The significantly enhanced lithium-storage capability of the Si@G network facilitates its application as an advanced anode material for LIBs with long cycle life and high energy and power density.

## AUTHOR INFORMATION

### Corresponding Authors

*E-mail: zjuwuping@njnu.edu.cn (P.W.).
*E-mail: zhouyiming@njnu.edu.cn (Y.Z.).

### Notes

The authors declare no competing financial interest.

## ACKNOWLEDGMENTS

We appreciate the financial support from the Natural Science Foundation of Jiangsu Province (BK20130900), the Natural Science Foundation of Jiangsu Higher Education Institutions of China (13KJB150026), the Industry-Academia Cooperation Innovation Fund Project of Jiangsu Province (BY2013001-01 and BY2012001), the Priming Scientific Research Foundation for Advanced Talents in Nanjing Normal University (2013103XGQ0008), and a project funded by the Priority Academic Program Development of Jiangsu Higher Education Institutions.

## REFERENCES

(1) Szczech, J. R.; Jin, S. Nanostructured silicon for high capacity lithium battery anodes. *Energy Environ. Sci.* **2011**, *4*, 56−72.
(2) Li, X.; Zhi, L. Managing voids of Si anodes in lithium ion batteries. *Nanoscale* **2013**, *5*, 8864−8873.

(3) McDowell, M. T.; Lee, S. W.; Harris, J. T.; Korgel, B. A.; Wang, C.; Nix, W. D.; Cui, Y. In situ TEM of two-phase lithiation of amorphous silicon nanospheres. *Nano Lett.* **2013**, *13*, 758−764.
(4) Hwa, Y.; Kim, W. S.; Yu, B. C.; Hong, S. H.; Sohn, H. J. Enhancement of the cyclability of a Si anode through $Co_3O_4$ coating by the sol−gel method. *J. Phys. Chem. C* **2013**, *117*, 7013−7017.
(5) Wang, J.; Du, N.; Song, Z.; Wu, H.; Zhang, H.; Yang, D. Synthesis of nanoporous three-dimensional current collector for high-performance lithium-ion batteries. *RSC Adv.* **2013**, *3*, 7543−7548.
(6) Chockla, A. M.; Bogart, T. D.; Hessel, C. M.; Klavetter, K. C.; Mullins, C. B.; Korgel, B. A. Influences of gold, binder and electrolyte on silicon nanowire performance in Li-ion batteries. *J. Phys. Chem. C* **2012**, *116*, 18079−18086.
(7) Fan, X.; Zhang, H.; Du, N.; Wu, P.; Xu, X.; Li, Y.; Yang, D. Vertically ordered $Ni_3Si_2$/Si nanorod arrays as anode materials for high-performance Li-ion batteries. *Nanoscale* **2012**, *4*, 5343−5347.
(8) Bao, Z.; Weatherspoon, M. R.; Shian, S.; Cai, Y.; Graham, P. D.; Allan, S. M.; Ahmad, G.; Dickerson, M. B.; Church, B. C.; Kang, Z.; Abernathy, H. W., III; Summers, C. J.; Liu, M.; Sandhage, K. H. Chemical reduction of three-dimensional silica micro-assemblies into microporous silicon replicas. *Nature* **2007**, *446*, 172−175.
(9) Xing, A.; Zhang, J.; Bao, Z.; Mei, Y.; Gordin, A. S.; Sandhage, K. H. A magnesiothermic reaction process for the scalable production of mesoporous silicon for rechargeable lithium batteries. *Chem. Commun.* **2013**, *49*, 6743−6745.
(10) Xing, A.; Tian, S.; Tang, H.; Losic, D.; Bao, Z. Mesoporous silicon engineered by the reduction of biosilica from rice husk as a high-performance anode for lithium-ion batteries. *RSC Adv.* **2013**, *3*, 10145−10149.
(11) Shen, L.; Guo, X.; Fang, X.; Wang, Z.; Chen, L. Magnesiothermically reduced diatomaceous earth as a porous silicon anode material for lithium ion batteries. *J. Power Sources* **2012**, *213*, 229−232.
(12) Wen, Z.; Lu, G.; Mao, S.; Kim, H.; Cui, S.; Yu, K.; Huang, X.; Hurley, P. T.; Mao, O.; Chen, J. Silicon nanotube anode for lithium-ion batteries. *Electrochem. Commun.* **2013**, *29*, 67−70.
(13) Lu, Z.; Zhu, J.; Sim, D.; Zhou, W.; Shi, W.; Hng, H. H.; Yan, Q. Synthesis of ultrathin silicon nanosheets by using graphene oxide as template. *Chem. Mater.* **2011**, *23*, 5293−5295.
(14) Liu, N.; Huo, K.; McDowell, M. T.; Zhao, J.; Cui, Y. Rice husks as a sustainable source of nanostructured silicon for high performance Li-ion battery anodes. *Sci. Rep.* **2013**, *3*, 1919.
(15) Xin, X.; Zhou, X.; Wang, F.; Yao, X.; Xu, X.; Zhu, Y.; Liu, Z. A 3D porous architecture of Si/graphene nanocomposite as high-performance anode materials for Li-ion batteries. *J. Mater. Chem.* **2012**, *22*, 7724−7730.
(16) Zhu, Y.; Liu, W.; Zhang, X.; He, J.; Chen, J.; Wang, Y. Directing silicon−graphene self-assembly as a core/shell anode for high-performance lithium-ion batteries. *Langmuir* **2013**, *29*, 744−749.
(17) Wang, X. L.; Han, W. Q. Graphene enhances Li storage capacity of porous single-crystalline silicon nanowires. *ACS Appl. Mater. Interfaces* **2010**, *2*, 3709−3713.
(18) Luo, J.; Zhao, X.; Wu, J.; Jang, H. D.; Kung, H. H.; Huang, J. Crumpled graphene-encapsulated Si nanoparticles for lithium ion battery anodes. *J. Phys. Chem. Lett.* **2012**, *3*, 1824−1829.
(19) Park, S. H.; Kim, H. K.; Ahn, D. J.; Lee, S. I.; Roh, K. C.; Kim, K. B. Self-assembly of Si entrapped graphene architecture for high-performance Li-ion batteries. *Electrochem. Commun.* **2013**, *34*, 117−120.
(20) Wang, B.; Li, X.; Luo, B.; Zhang, X.; Shang, Y.; Cao, A.; Zhi, L. Intertwined network of Si/C nanocables and carbon nanotubes as lithium-ion battery anodes. *ACS Appl. Mater. Interfaces* **2013**, *5*, 6467−6472.
(21) Wang, B.; Li, X.; Zhang, X.; Luo, B.; Jin, M.; Liang, M.; Dayeh, S. A.; Picraux, S. T.; Zhi, L. Adaptable silicon−carbon nanocables sandwiched between reduced graphene oxide sheets as lithium ion battery anodes. *ACS Nano* **2013**, *7*, 1437−1445.
(22) Xue, L.; Xu, G.; Li, Y.; Li, S.; Fu, K.; Shi, Q.; Zhang, X. Carbon-coated Si nanoparticles dispersed in carbon nanotube networks as anode material for lithium-ion batteries. *ACS Appl. Mater. Interfaces* **2013**, *5*, 21−25.
(23) Li, Y.; Xu, G.; Xue, L.; Zhang, S.; Yao, Y.; Lu, Y.; Toprakci, O.; Zhang, X. Enhanced rate capability by employing carbon nanotube-loaded electrospun Si/C composite nanofibers as binder-free anodes. *J. Electrochem. Soc.* **2013**, *160*, A528−A534.
(24) Xue, L.; Fu, K.; Li, Y.; Xu, G.; Lu, Y.; Zhang, S.; Toprakci, O.; Zhang, X. Si/C composite nanofibers with stable electric conductive network for use as durable lithium-ion battery anode. *Nano Energy* **2013**, *2*, 361−367.
(25) Fan, Y.; Zhang, Q.; Lu, C.; Xiao, Q.; Wang, X.; Tay, B. K. High performance carbon nanotube−Si core−shell wires with a rationally structured core for lithium ion battery anodes. *Nanoscale* **2012**, *3*, 1503−1506.
(26) Han, S.; Wu, D.; Li, S.; Zhang, F.; Feng, X. Graphene: A two-dimensional platform for lithium storage. *Small* **2013**, *9*, 1173−1187.
(27) Li, J.; Wu, P.; Tang, Y.; Xu, X.; Zhou, Y.; Chen, Y.; Lu, T. Three-dimensional mesoporous Sn−Ni@C network derived from cyanogel coordination polymers: Towards high-performance anodes for lithium storage. *CrystEngComm* **2013**, *15*, 10340−10345.
(28) Shen, L.; Zhang, X.; Li, H.; Yuan, C.; Cao, G. Design and tailoring of a three-dimensional $TiO_2$−graphene−carbon nanotube nanocomposite for fast lithium storage. *J. Phys. Chem. Lett.* **2011**, *2*, 3096−3101.
(29) Wang, X. L.; Han, W. Q.; Chen, H.; Bai, J.; Tyson, T. A.; Yu, X. Q.; Wang, X. J.; Yang, X. Q. Amorphous hierarchical porous $GeO_x$ as high-capacity anodes for Li ion batteries with very long cycling life. *J. Am. Chem. Soc.* **2011**, *133*, 20692−20695.
(30) Shen, L.; Uchaker, E.; Yuan, C.; Nie, P.; Zhang, M.; Zhang, X.; Cao, G. Three-dimensional coherent titania−mesoporous carbon nanocomposite and its lithium-ion storage properties. *ACS Appl. Mater. Interfaces* **2012**, *4*, 2985−2992.
(31) Stober, W.; Fink, A. Controlled growth of monodisperse silica spheres in micron size range. *J. Colloid Interface Sci.* **1968**, *26*, 62−69.
(32) Du, N.; Zhang, H.; Yang, D. One-dimensional hybrid nanostructures: synthesis via layer-by-layer assembly and applications. *Nanoscale* **2012**, *4*, 5517−5526.
(33) Ji, H.; Zhang, L.; Pettes, M. T.; Li, H.; Chen, S.; Shi, L.; Piner, R.; Ruoff, R. S. Ultrathin graphite foam: A three-dimensional conductive network for battery electrodes. *Nano Lett.* **2012**, *12*, 2446−2451.
(34) Kim, T.; Jung, G.; Yoo, S.; Suh, K. S.; Ruoff, R. S. Activated graphene-based carbons as supercapacitor electrodes with macro- and mesopores. *ACS Nano* **2013**, *7*, 6899−6905.
(35) Kovalenko, I.; Zdyrko, B.; Magasinski, A.; Hertzberg, B.; Milicev, Z.; Burtovyy, R.; Luzinov, I.; Yushin, G. A major constituent of brown algae for use in high-capacity Li-ion batteries. *Science* **2011**, *334*, 75−79.
(36) Guo, J.; Wang, C. A polymer scaffold binder structure for high capacity silicon anode of lithium-ion battery. *Chem. Commun.* **2010**, *46*, 1428−1430.
(37) Erk, C.; Brezesinski, T.; Sommer, H.; Schneider, R.; Janek, J. Toward silicon anodes for next-generation lithium ion batteries: A comparative performance study of various polymer binders and silicon nanopowders. *ACS Appl. Mater. Interfaces* **2013**, *5*, 7299−7307.